Preliminary parameter characterization for numerical optimization of ducted propellers

Margot Remaud, Pierre-Michel Guilcher, Jean-Marc Laurens

Maritime Technology and Research

https://www.tci-thaijo.org/index.php/MTR

Preliminary parameter characterization for numerical optimization of ducted propellers

Margot Remaud, Pierre-Michel Guilcher and Jean-Marc Laurens*
ENSTA Bretagne, IRDL, 2 rue François Verny, 29806 Brest, France

Article information
Received: April 13, 2019
Revised: May 18, 2019
Accepted: May 21, 2019

Keywords
Ducted propeller
Potential flow
Design
Optimization

Abstract
In this paper, a preliminary parameter characterization for the numerical optimization of ducted propellers was performed. The ENSTA Bretagne in-house solver used is based on the potential flow theory. Although the potential flow solver is able to solve unsteady problems, in this preliminary study, only steady state flow problems are considered. Different parameters are analyzed, such as the gap between the propeller tip and the inner duct surface, as well as the propeller location in the duct tube. The analyses are carried out on a standard advance coefficient range. A quick study shows that a neutral NACA profile for the duct section can provide higher performance predictions than the classical accelerating Kort nozzle 19A. The parameter study shows that the best axial position for the rotor is not necessarily near the duct entrance and, more importantly, that a thinner duct profile can give better hydrodynamic performance.

1. Introduction

Since 1960, the characterization and the design of ducted propellers have been the subjects of ongoing studies. One of the first fundamental papers, written by Morgan (1961), provided a ducted propeller analysis by modelling the duct according to the lifting line theory. In the late 1960s, Van Manen (1970) published an eminent paper on accelerating ducts and Kaplan propellers. Kerwin et al. (1987) published a fundamental analysis of the numerical modelling of ducted propellers . This study aimed to explain the use of potential flow theory in blade, hub, and duct numerical modelling. The panel code generated a complex mesh with helical panels named “extravaganza” by the authors. Subsequently, further research was carried out on this topic by Baltazar and Falcão de Campos (2009), Baltazar et al. (2012), and Laurens et al. (2012). Some research on the duct design demonstrated that ducted propellers are interesting in high loading blade conditions, such as fishing vessels (Dasira and Laurens, 2014). Despite these first interesting results concerning economic and environmental points of view, few papers have been published on the optimization of ducted propellers, such as the Kort nozzles 19A, 22, and 37, which were developed by the Maritime Research Institute of the Netherlands and reported by Kuiper (1992). A recent paper by Gaggero et al. (2017) on the study of ducted propeller characteristics deserves to be cited. Their study aimed to characterize the flow swallowing in decelerating ducts, and how it influences propeller behavior. Finally, few studies have been conducted on the characterization of parameters for ducted propeller design. This paper focuses on 3 ducted propellers, using only one rotor type: the Kaplan 4.55 bare

*Corresponding author: ENSTA Bretagne, IRDL, 2 rue François Verny, 29806 Brest, France
E-mail address: jean-marc.laurens@ensta-bretagne.fr

propeller. The rotor diameter is fixed to one meter. The 19A, NACA0017, and NACA0008 ducts are studied regarding different configurations, presented in section 3. Parameter variance involved in this study are the Gap-to-propeller radius ratio, the duct thickness-to-chord ratio, and the propeller axial position, as detailed in the diagram of **Figure 1**.

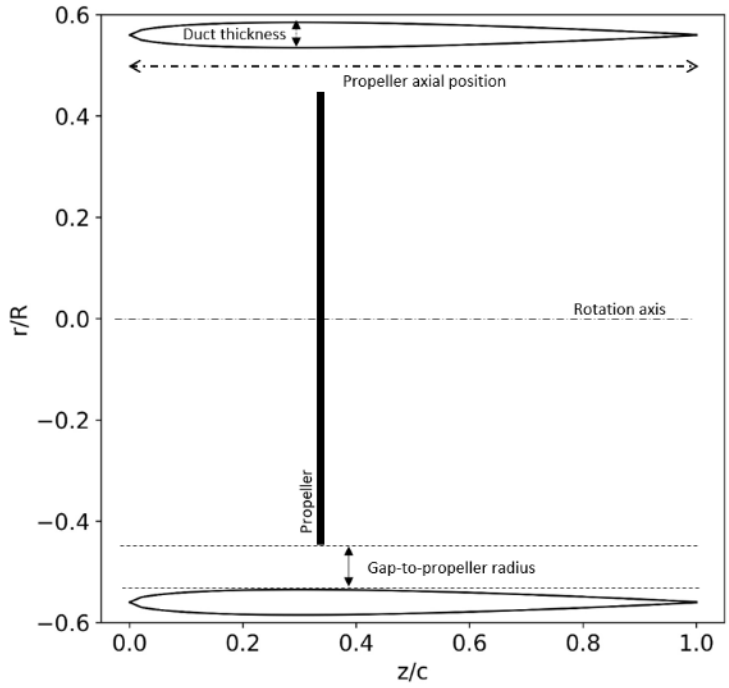

Figure 1 Parameters involved in the study.

2. Materials and methods

The Kort nozzle 19A, described in Kuiper (1992), is widely used by the maritime industry when ducts are required for their performance. Several papers have been published on potential theory model validation, as in Baltazar et al. (2012) for the potential flow theory solver of the Maritime Research Institute of Netherlands, or Baltazar and Rijpkema (2013) for the in-house panel code of the Instituto Superior Técnico de Lisboa. These papers provide information on some assumptions to comply with and validate their code with the widely-used Kort nozzle 19A. Accordingly, validation of the ENSTA Bretagne in-house panel code are carried out with the same nozzle.

2.1 Frame

The duct and the propeller are defined in the same frame, as shown in **Figure 2**. As the hub does not significantly influence the hydrodynamic coefficients, according to the results of Laurens et al. (2012), it is not simulated in this ongoing analysis. The hub space is therefore left empty.

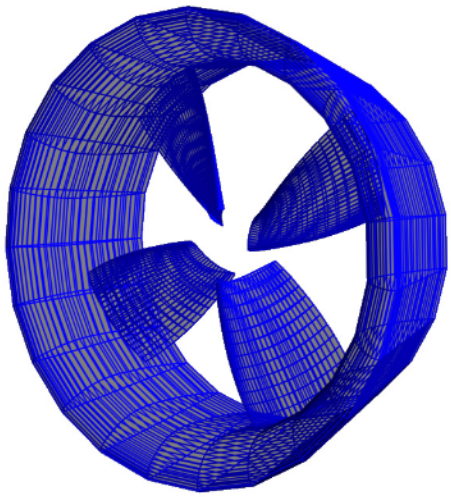

Figure 2 Example of mesh; Kaplan propeller Ka55 in 19A Kort nozzle.

2.2 Mathematical model

The flow is assumed incompressible, inviscid, and irrotational. In line with these hypotheses, the velocity vector is the derivative of a potential function φ, the continuity equation is reduced to the Laplace equation for the potential function, and the momentum equations are reduced to the Bernoulli equation. The potential function ϕ for the exterior problem must verify the Laplace equation in the domain D_e, a radiation condition at infinity, together with the no penetration condition on the surface ∂D_e of the bodies (Eqs. (1) and (2));

$$\Delta\varphi = 0 \qquad x \in D_e \tag{1}$$

$$\frac{\partial\varphi}{\partial n} = 0 \qquad x \in \partial D_e \tag{2}$$

The potential function is expressed here in a frame moving with the body. By using Green's identities, the potential function inside the fluid domain is only dependent on its value (Dirichlet condition) and its derivative value (Neumann condition) on the boundaries. These boundary conditions are fulfilled with a distribution of singularities, either sources or dipoles. For any point P on the body surface, Green's identity provides (Eq. (3));

$$\frac{\varphi(P)+\varphi_i(P)}{2} = \frac{1}{4\pi}\int_{S_B \cup S_W}\left[\frac{1}{r}\nabla(\varphi-\varphi_i) - (\varphi-\varphi_i)\nabla\left(\frac{1}{r}\right)\right]\cdot \boldsymbol{n}dS + \varphi_\infty(P) \tag{3}$$

where ϕ and ϕi stand respectively for the exterior and interior velocity potential, and φ_∞ is the incident potential corresponding to the incoming flow. The integral is performed on the bodies and wake surfaces. The source and dipole distributions are identified as $\sigma = \nabla(\varphi - \varphi_i)\cdot n$ and $\mu = -(\varphi - \varphi_i)$.

The code we use belongs to what Hoeijmakers (1992) refers to as "second generation" panel methods involving the specification of the interior potential. In this particular case, φ_i equal to φ_∞, the problem reduces to the determination of the dipole distribution on the body surface and the wake (Eq. (4));

$$\frac{\mu(P)}{2} - \frac{1}{4\pi}\int_{S_B \cup S_W} \mu(Q)\nabla\left(\frac{1}{r}\right)\cdot \boldsymbol{n} dS = \frac{1}{4\pi}\int_{S_B} \frac{\sigma(Q)}{r} dS \quad (4)$$

This corresponds to a Fredholm integral equation of the second kind.

The source distribution is solely determined by the slip condition, yielding (Eq. (5));

$$\sigma(P) = -V_\infty(P)\cdot \boldsymbol{n} \quad (5)$$

To close the system and provide a physical solution, a Kutta condition linking the dipole distribution in the wake to the dipole distribution on the lifting bodies must be enforced. Indeed, for a lifting body such as a wing, a propeller blade, or a duct, the slip condition is not sufficient since, theoretically, a body in an inviscid fluid flow does not produce any hydrodynamic forces. To mimic the behavior of viscous fluid flow around a lifting body, an additional condition is required. This consists of forcing the flow to be lined up with the trailing edge. In the present case, the Kutta condition is expressed in an implicit form, with pressure equality on both sides of the trailing edge. Once the intensities of the singularities have been determined, taking the boundary conditions into account, the velocities and the pressure can be computed anywhere in the fluid domain.

2.3 Numerical model

Body surfaces are discretized into first order panels carrying constant source and doublet distributions. The wake developing behind the propeller or the rudder is formed with a sheet of first order panels carrying constant doublet distributions, and is generated over time in a Lagrangian manner. The choice of interior potential, imposing the slip condition on the body surface, determines the sources directly from the inlet velocity and the normal vectors. Hence, the unknowns of the problem are the dipoles.

The integral equation is solved with a collocation method, where the collocation points correspond to the center of each element. Moreover, the Kutta condition is nonlinear, resulting in a global nonlinear problem. The resolution is based on a Gauss-Seidel iterative scheme with a block matrices approach, where the unknowns are the dipole strengths on the lifting surfaces and the first row in the wake. The convergence is generally achieved in 3 to 5 iterations. Once the dipole strengths are determined, the velocity potential, and thus the velocity and pressure, are computed on the different surfaces to provide the global forces and moments. At each time step, the wake sheet is updated with a Euler forward scheme. The locations of the sheet panel vertices are recalculated, but not the dipoles they carry. Consequently, a new row of panels is released in the wake, immediately adjacent to the trailing edge, whose dipole strength is determined through the imposition of the Kutta condition. The computation is repeated a sufficient number of time steps to develop the vortex wake behind the lifting surfaces and achieved converged results on forces.

Non-lifting bodies, such as the hub, are discretized using first-order panels carrying constant source and dipole distributions. The propeller hub can be easily modelled this way, but in most cases it does not influence the hydrodynamic coefficients so, in the results presented here, we do not simulate its presence. The code allows for unsteady state flow simulation, and the body thickness representation leads to an accurate distribution of pressure coefficients (Cp) on duct and blade surfaces. From the velocities, we compute the local Reynolds number, R_n, on each surface panel, which provides the local friction coefficient, C_f, using standard formulae;

$0.027/\sqrt[7]{R_n}$ for turbulent flow, and $0.664/\sqrt{R_n}$ for laminar flow. The transition is forced at R_n=5×10^5.

The boundary element methods only require a surface mesh of the solid objects. We developed a friendly user mesh generator for the blade and duct surfaces. A typical mesh is presented in **Figure 2**. In this example, we also show the wake which has been automatically generated by the

potential flow code. Since the propeller blades and the duct are computed as lifting bodies, they must present a sharp trailing edge from which the wake, modelled as a sheet of first order panels carrying constant doublet distributions, originates.

The procedure consists of separating the flow around the propeller and the flow around the duct into 2 different runs. A similar strategy has already been used for pods and rudders. Once the flow around the duct has been solved, we compute the duct-induced velocities at the blade control points (i.e., the centers of all panels). The flow around the propeller is then computed in the presence of the duct-induced velocities. We then compute the propeller-induced velocities on the surface of the duct. The procedure is repeated until convergence, which occurs after only a few iterations. The procedure allows for much simpler meshes than the one used by Kerwin et al. (1987) or by Baltazar et al. (2009).

2.4 Coefficients used

As commonly used in propulsive efficiency prediction, the advance coefficient is defined as given below (Eq. (6)). Index p stands for the propeller characteristics, while index d stands for the duct characteristics, and index T stands for the total ducted propeller characteristics.

$$J = \frac{V_\infty}{n.D_p} \tag{6}$$

The thrust and torque coefficients of the bare propeller are defined as (Eq. (7));

$$K_{Tp} = \frac{T_p}{\rho n^2 D_p^4} \quad K_{Qp} = \frac{Q_p}{\rho n^2 D_p^5} \tag{7}$$

To be consistent with the bare propeller thrust coefficient definition, the duct thrust coefficient is defined as (Eq. (8));

$$K_{Td} = \frac{T_d}{\rho n^2 D_p^4} \tag{8}$$

Linearly, from both the duct and the bare propeller, the total thrust coefficient is defined as (Eq. (9));

$$T_T = T_p + T_d \tag{9}$$

As the duct does not rotate, the total torque is composed only of the propeller torque, Q_p.

2.5 Circulation

The sides of lifting bodies, such as wings, propeller blades, or ducts, are respectively called the suction side and the pressure side. For an accelerating duct profile, the suction side is the inner side, while the pressure side is the outer side. The in-house potential code provides the fluid velocities contribution at each point of the domain. This is explained by the circulation, Γ, which is defined as (Eq. (10));

$$\Gamma = \oint_\Omega \bar{V}.\overline{ds}, \tag{10}$$

and which is related to the lift by the Joukowski relation (Eq. (11));

$$= -\rho V \Gamma \tag{11}$$

The velocity difference, ΔV, inside and outside of the duct, can be assessed using a heuristic reasoning. We suppose that the fluid velocity distribution on each side of the section is constant. We suppose that it is equal to V_∞ outside the duct, and equal to $V_\infty + \Delta V$ inside the duct. ΔV can be either positive or negative. The circulation around a blade can be calculated as given below (Eq. (12));

$$\Gamma = (V_\infty + \Delta V)c - V_\infty c = c \times \Delta V \tag{12}$$

V_∞ stands for the incoming flow velocity, ΔV is the induced velocity, and c stands for the wing profile chord. This allows us to deduct a simple expression for the velocity difference as a function of the duct section lift coefficient, C_L (Eq. (13));

$$C_L = 2\frac{\Delta V}{V_\infty} \tag{13}$$

This crude reasoning gives a very rough estimate of the velocity inside the standalone duct.

2.6 Duct section trailing edge

The 19A duct section does not present a sharp trailing edge. Baltazar and Falcão de Campos (2009) performed simulations changing the wake shedding location on the 19A round trailing edge. These results are confirmed by the experimental study performed by Kotsonis et al. (2014). Both studies concluded that the wake shedding location has a significant effect on the duct thrust. To apply the Kutta condition simply, the ducts computed in studies have a sharp trailing edge, as in Baltazar et al. (2012). The 19A-sharp profile used was derived from Kuiper's book (1992). Both profiles, the sharp one and the original 19A, are presented in **Figure 3**.

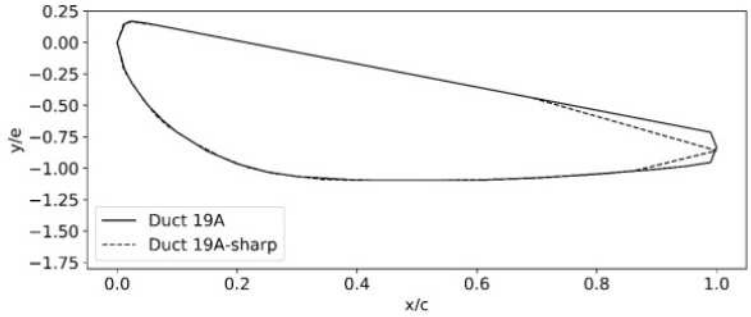

Figure 3 Original 19A duct profile and adapted 19A-sharp profile.

2.7 Propeller loss of efficiency

In actuator disk theory, a maximum efficiency is derived from the loss of kinetic energy. The propeller is modelled by a disk with a sudden pressure jump. By applying the Bernoulli equation on a semi-infinite streamlines on each side of the actuator disk, we find that the ratio between the downstream wake and the upstream wake to be: $\sqrt{1 + C_{Th}}$, where C_{Th} is the thrust loading coefficient, defined as (Eq. (14));

$$C_{Th} = \frac{T}{0.5.\rho.U_\infty^2.A_P} \tag{14}$$

From this simple model, we therefore obtain the theoretical loss of efficiency due to kinetic energy in the wake. This gives the maximum efficiency $\bar{\eta}$ for a bare propeller to be (Eq. (15));

$$\bar{\eta} = \frac{2}{1+\sqrt{1+C_{Th}}} \tag{15}$$

The same procedure also gives the maximum efficiency for a ducted propeller (Eq. (16));

$$\bar{\eta} = \frac{2}{1+\sqrt{1+\tau.C_{Th}}} \tag{16}$$

where τ is the ratio of the additional thrust given by the duct T_D over the total thrust T_T. The addition of a duct is the only way to reduce $\bar{\eta}$. Heavily loaded propellers, such as those of trawlers during the trawling mode, always benefit from such a duct.

There are 2 additional major factors which cause the loss of energy: loss due to fluid rotation, and loss due to friction. These can easily be separated using the BEM code, since the friction forces are added to the pressure forces. **Figure 4** presents the decomposition of the efficiency loss due to friction, rotation, and kinetic energy as a function of the thrust loading coefficient C_{Th} for a standard propeller.

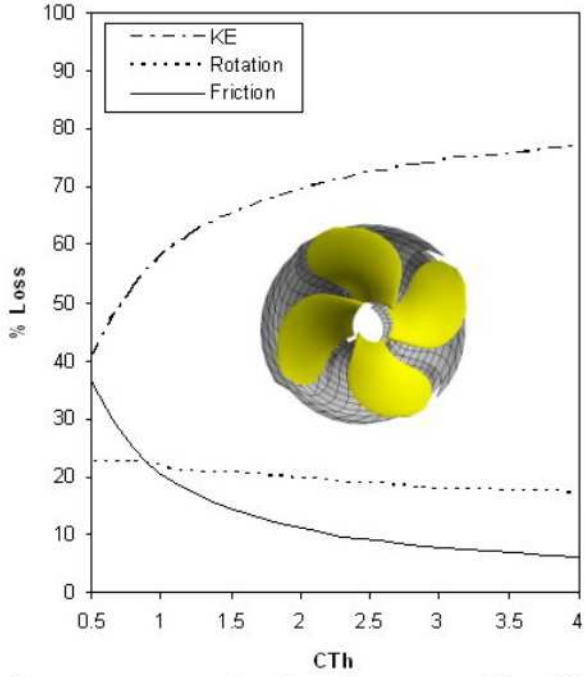

Figure 4 Percentage loss of energy versus C_{Th} for a bare propeller. The kinetic energy loss (KE) becomes dominant when the thrust loading coefficient, C_{Th}, is important.

Subsequently, a large number of simulations are performed to assess whether the curves of **Figure 4** apply to any propeller. Many different propellers, with different aspect ratios, numbers of blades, and geometrical laws defining the propeller geometry, are considered. It appears that the parameter which presents the most significant impact on these curves is the section maximum camber. In all cases, the kinetic energy loss becomes rapidly dominant when the propeller loading is increased.

3. Results and discussion

In the previous section, the role of the duct, and its importance in increasing the efficiency of propulsion when the propeller is heavily loaded, was presented, as well as the numerical tools used in the study. There are numerous parameters involved in the performance of ducted propellers. We

report the effects of only some of these in this article, and mainly analyze the physics underlying the behavior.

3.1 Duct shapes, propeller axial position and gap-to-propeller radius ratio

As a reference, the Kaplan 4.55 propeller is the propeller used in every ducted propeller running case. At this stage, we concentrate our study on the duct shape and on the position of the propeller.

3.1.1 Duct profile: NACA0017

As the purposes of this study are to assess the performance of the Kort nozzle 19A and to identify which parameter could improve the propulsive performance of a duct, a different shape is also studied: the NACA0017. In view of the fact that the 19A profile has a thickness-to-chord ratio equal to 16.667 %, it was decided to study a neutral NACA profile with the same thickness-to-chord ratio, which is written as "NACA0017"; see **Figure 5**. In this way, it was decided to keep the same thickness-to-chord ratio between both profiles, and to keep the same chord.

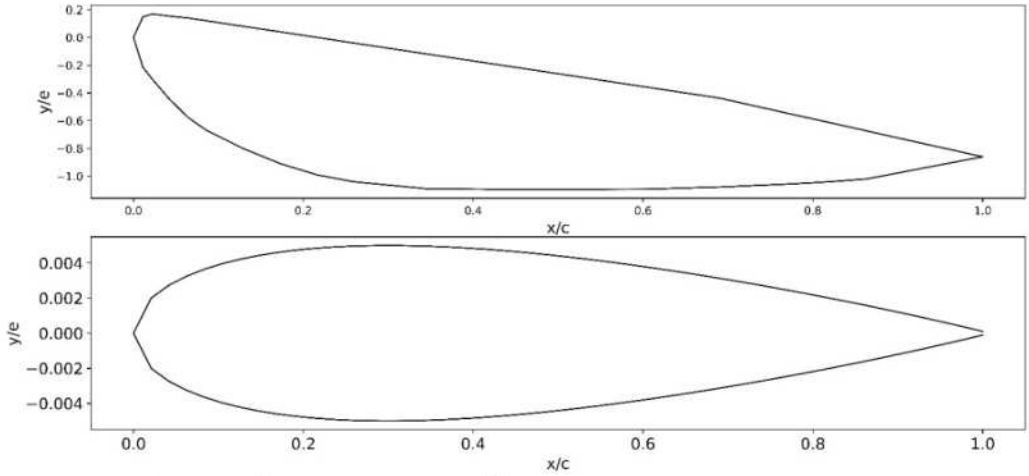

Figure 5 Ducts 19A-sharp and NACA0017 profiles.

Four configurations are examined: the standard Kort nozzle 19A, as described in Kuiper (1992), and the NACA0017, with 3 different positions of the propeller. These 3 cases are named NACA0017-a, NACA0017-b, and NACA0017-c, and are described in **Table 1**. We use the size of the Kaplan 4.55 as in Saari (2014), with P/D=1.

Table 1 Configurations.

Profile	Gap/Propeller radius	Chord/Duct diameter	Propeller axial position
19A-sharp	3.10 %	48 %	1/3
NACA0017-a	3.10 %	53 %	1/3
NACA0017-b	7.00 %	51 %	1/3
NACA0017-c	7.00 %	51 %	7/12

The results of the simulations are summarized in **Table 2**.

Table 2 Performance prediction summary for 4 configurations using NACA0017.

Profile	Efficiency for J=0.5	Maximum efficiency	Advance coefficient corresponding to maximum efficiency
19A-sharp	58 %	65 %	0.70
NACA0017-a	58 %	67 %	0.70
NACA0017-b	58 %	68 %	0.70
NACA0017-c	62 %	75 %	0.80

The complete results are provided in **Table 3**. As expected, the duct contribution to the thrust force increases as J is lower, because of the increasing acceleration provided by the propeller when it is heavily loaded. At higher values of J, the duct does not provide any additional thrust, and eventually presents more drag than thrust. The procedure we present here aims to optimize the ducted propeller geometry and, once the optimization loop is perfectly mastered, CFD and experimental trials will be necessary to complete and confirm the progress. The NACA0017-c clearly presents the best performances.

Table 3 Complete performance predictions for 4 configurations using the NACA0017.

	19A-sharp			NACA0017-a			NACA0017-b			NACA0017-c		
J	KtD	KtP	Eta	KtD	Kt	Eta	KtD	Kt	Eta	KtD	Kt	Eta
0.45	0.035	0.209	0.540	0.035	0.238	0.537	0.037	0.245	0.543			
0.5	0.027	0.193	0.576	0.028	0.215	0.575	0.031	0.222	0.583	0.047	0.288	0.624
0.55	0.020	0.177	0.606	0.023	0.191	0.609	0.025	0.198	0.617	0.039	0.259	0.662
0.6	0.014	0.161	0.630	0.018	0.168	0.637	0.019	0.174	0.645	0.031	0.230	0.695
0.65	0.008	0.144	0.647	0.013	0.144	0.656	0.014	0.150	0.666	0.024	0.200	0.721
0.7	0.003	0.126	0.652	0.009	0.120	0.665	0.010	0.126	0.677	0.018	0.171	0.739
0.75	-0.003	0.111	0.641	0.005	0.096	0.659	0.006	0.102	0.673	0.012	0.143	0.747
0.8	-0.006	0.089	0.621	0.002	0.073	0.632	0.003	0.078	0.650	0.007	0.114	0.742
0.85	-0.009	0.070	0.569	0.000	0.049	0.564	0.000	0.054	0.591	0.003	0.086	0.716
0.9	-0.011	0.050	0.470	-0.002	0.024	0.410	-0.002	0.029	0.459	0.000	0.059	0.651

The results show that a neutral NACA profiles can provide higher performance predictions than the accelerating Kort nozzle 19A. A smaller gap slightly changes the maximum circulation along the propeller blade but does not prevent the tip vortex and the resultant 3D effect. This observation explains why the NACA0017-a is not more efficient than the NACA0017-b. The best axial position for the propeller is not at the maximum duct section thickness. We will explain why, but we will first examine the effect of the duct section maximum thickness.

3.1.2 Duct profile: NACA0008

As illustrated by the curves of **Figure 4**, an important loss of efficiency in kinetic energy is observed when the propeller is heavily loaded. If the propeller is too heavily loaded, it is because it is too small compared to the thrust it has to deliver. The duct is the device that allows the partial transfer of the thrust from the propeller to the duct. Because of the lack of space, the maximum diameter of the entire system has to be kept constant. Therefore, adding a duct will reduce the propeller diameter, especially if it has a large maximum thickness. The series of configurations

examined in the previous section are repeated using a duct profile with a lesser maximum thickness, the NACA0008. The performance prediction summary is shown in **Table 4**.

Table 4 Performance prediction summary.

Profile	Efficiency for J=0.5	Maximum efficiency	Advance coefficient corresponding to maximum efficiency
19A-sharp	58 %	65 %	0.70
NACA0008-a	57 %	65 %	0.70
NACA0008-b	60 %	73 %	0.75
NACA0008-c	64 %	79 %	0.80

The complete results are shown in **Table 5**. As expected, the hierarchy of the results is the same as previously; however, the values are slightly higher. These results tend to show that not only does reducing the duct section thickness increase the propeller diameter, but it also ensures a better performance.

Table 5 Performance predictions for the 4 configurations using NACA0008.

	19A-sharp			NACA0008-a			NACA0008-b			NACA0008-c		
J	**KtD**	**KtP**	**Eta**	**KtD**	**KtP**	**Eta**	**KtD**	**KtP**	**Eta**	**KtD**	**KtP**	**Eta**
0.45	0.035	0.209	0.540							0.057	0.273	0.587
0.50	0.027	0.193	0.576	0.025	0.180	0.565	0.036	0.207	0.599	0.056	0.256	0.644
0.55	0.020	0.177	0.606	0.020	0.162	0.598	0.030	0.190	0.636	0.045	0.235	0.681
0.60	0.014	0.161	0.630	0.015	0.144	0.624	0.024	0.172	0.669	0.036	0.213	0.714
0.65	0.008	0.144	0.647	0.011	0.125	0.641	0.019	0.154	0.696	0.029	0.192	0.743
0.70	0.003	0.126	**0.652**	0.007	0.105	**0.648**	0.014	0.136	0.715	0.022	0.169	0.766
0.75	-0.003	0.111	0.641	0.004	0.085	0.640	0.010	0.116	**0.726**	0.016	0.146	0.781
0.80	-0.006	0.089	0.621	0.001	0.065	0.605	0.007	0.097	0.724	0.011	0.123	**0.786**
0.85	-0.009	0.070	0.569	-0.001	0.043	0.525	0.004	0.076	0.704	0.007	0.100	0.778
0.90	-0.011	0.050	0.470	-0.003	0.020	0.333	0.002	0.055	0.651	0.004	0.077	0.746

Finally, to understand why the axial position of the propeller in the duct provides a better efficiency when it is situated aft of the maximum duct section thickness, we have to examine the pressure distribution on the duct surface with the presence of the propeller. In **Figure 6**, a comparison of the pressure distribution, Cp, as defined by the ITTC (2011), on the duct section for the Kort nozzle 19A and the NACA0008-c at J=0.5 and at J=0.8 is presented. When we examine the negative Cp values on the suction side from the leading edge, we note that they are spread across a longer part of the chord for the NACA0008-c than for the 19A. Now, if we look at the profiles in **Figure 6**, the negative Cp will generate some lift up to 30 % chord. It is therefore not surprising that the NACA008-c performs better than the 19A. Furthermore, at J=0.5, we observe that the positive Cp on the inner duct surface after 50 % chord will provide some additional duct thrust. These last results indicate why the geometry of the duct and the axial position of the propeller are the key parameters to adjust in order to obtain a better performance. This conclusion is confirmed by the examination of the pressure distribution on the duct section for the 3 configurations using the NACA0008 profile. The hierarchy of the performances obtained in **Table 5** can be understood from the curves of **Figure 7**.

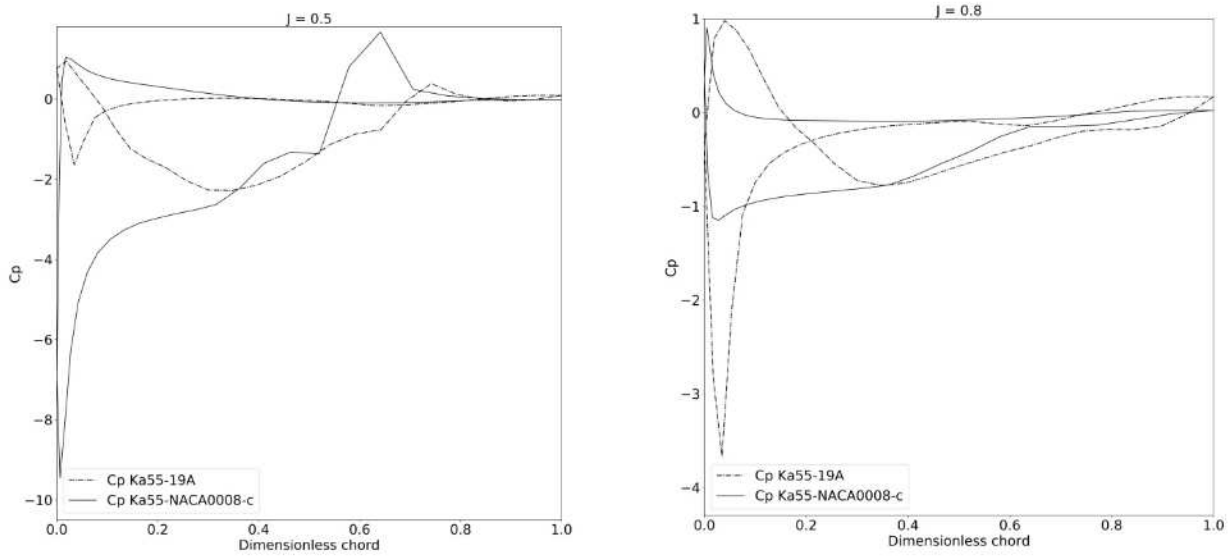

Figure 6 Compared pressure distribution on duct section for Kort nozzle 19A and NACA0008-c at J=0.5 (left) and at J=0.8 (right).

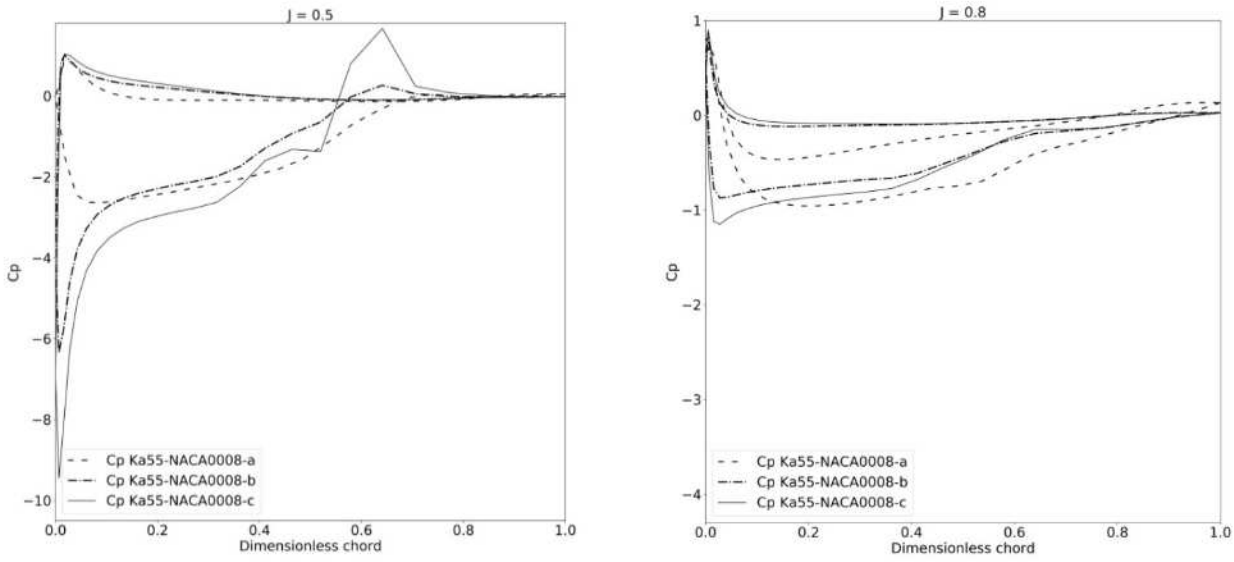

Figure 7 Compared pressure distribution on duct section for NACA0008-a,-b, and -c; at J=0.5 (left) and at J=0.8 (right).

4. Conclusions

This preliminary analysis provides interesting perspectives on improving ducted propeller efficiency and performance predictions. A performing potential flow procedure allows for rapid computation, and many configurations have been tested. The results presented in this paper show that a ducted propeller can be made more efficient by changing the geometry of the duct and the position of the rotor.

Further studies must be conducted to complete parameter characterization. In this study, only the duct section maximum thickness variation was considered, and it is clear that other geometric parameters, such as the camber, will be of influence on the performance of the ducted propeller. Hence, calculations should be performed to determine the influence of the gap-to-propeller radius

ratio, the chord-to-diameter ratio, the thickness-to-chord ratio, and the position-to-duct chord ratio. Furthermore, the velocity distribution in the duct tube was only briefly touched upon. Further computations and analyses should be carried out to deepen our understanding of this issue. Once ae complete analysis of the duct geometry is performed, we will optimize the blade propeller geometry and develop an iterative optimization tool to increase the performance. Finally, all the simulations performed in the present academic study consider a constant diameter for the rotor, namely one meter. For real application, the overall diameter should be kept constant.

References

Baltazar, J., & Falcao de Campos, J.A.C. (2009). *On the modeling of the flow in ducted propellers with a panel method*. Norway: Trondheim.

Baltazar, J., Falcão de Campos, J. A. C., & Bosschers, J. (2012). Open-water thrust and torque predictions of a ducted propeller system with a panel method. *International Journal of Rotating Machinery 2012*, 474785. doi:10.1155/2012/474785

Baltazar, J., Rijpkema, D., Falcao de Campos, J. A. C., & Bosschers, J. (2013). *A comparison of panel method and RANS calculations for a ducted propeller system in open-water*. In Third International Symposium on Marine Propulsors, Launceston, Tasmania, Australia.

Bosschers, J., Willemsen, C., Peddle, A., & Rijpkema, D. (2015). Analysis of ducted propellers by combining potential flow and RANS methods. In Fourth International Symposium on Marine Propulsors.

Coache, S., & Laurens, J. M. (2014). *Trawler duct propeller design: From systematic series to CFD*. In 3rd International Symposium on Fishing Vessel Energy Efficiency.

Dasira, A., & Laurens, J. M. (2014). Energy efficiency analysis of trawlers: Case study on an Indonesian trawler. *Indonesian Scholar Journal 1*(1), 245-250. doi:10.12962/ j23546026.y2014i1.202

Gaggero, S., Villa, D., Tani, G., Viviani, M., & Bertetta, D. (2017). Design of ducted propeller nozzles through a RANSE-based optimization approach. *Ocean Engineering 145*, 444-463. doi:10.1016/j.oceaneng.2017.09.037

Hoeijmakers, H. W. M. (1992). *Panel methods for aerodynamic analysis and design*. Washington, DC: National Aeronautics and Space Administration.

Kerwin, J. E., Kinnas, S. A., Lee, J. T., & Shih, W. Z. (1987). A surface panel method for the hydrodynamic analysis of ducted propellers. *Transaction SNAME 95*, 1-22.

Kotsonis, M., Pul, R., & Veldhuis, L. (2014). Influence of circulation on a rounded-trailing-edge airfoil using plasma actuators. *Experiments in Fluids 55*(7), 1772. doi:10.1007/s00348-014-1772-y

Kuiper, G. (1992). *The Wageningen Propeller series*. Wageningen: Marin Publication.

Laurens, J. M., Deniset F., & Moyne, S. (2012). *A BEM method for the hydrodynamic analysis of fishing boats propulsive systems*. In Second International Symposium on Fishing Vessel Energy Efficiency. Vigo, Spain.

Laurens, J. M., Leroux, J. B., & Coache, S. (2013). *Design and retrofit of the propulsion of trawlers to improve their efficiency*. Spain: A Coruna.

Morgan, W. B. (1961). *A theory of the ducted propeller with a finite number of blades*. University of California Report, Berkeley, California.

Saari, A. (2014). *Hydrodynamic study on a ducted propeller in a large vessel by time-accurate self-propulsion simulation with Reynolds-Averaged Navier-Stokes-equations*. (Master Thesis). Aalto University, Helsinki, Finland.

Van Manen, J. D. (1970). *Wake adapted ducted propellers*. Wageningen: H. Veenman & Zonen.